SAND2015-5520J

Three-Dimensional Fully-Coupled Electrical and Thermal Transport Model of Dynamic Switching in Oxide Memristors

X. Gao[a], D. Mamaluy[a], P. R. Mickel[a], and M. Marinella[a]

[a] Sandia National Laboratories, Albuquerque, New Mexico 87123, USA

We present a fully-coupled electrical and thermal transport model for oxide memristors that solves simultaneously the time-dependent continuity equations for all relevant carriers together with the time-dependent heat equation including Joule heating sources. The model captures all the important processes that drive memristive switching and is applicable to simulate switching behavior in a wide range of oxide memristors. The model is applied to simulate the ON switching in a 3D filamentary TaOx memristor. Simulation results show that, for uniform vacancy density in the OFF state, vacancies fill in the conduction filament till saturation, and then fill out a gap formed in the Ta electrode during ON switching; furthermore, ON-switching time strongly depends on applied voltage and the ON-to-OFF current ratio is sensitive to the filament vacancy density in the OFF state.

Introduction

Transition metal oxide memristors have recently attracted special attention from the semiconductor industry and academia. Memristors are one of the strongest candidates to replace flash, and possibly DRAM and SRAM in the nearest future (1,2). Moreover, memristors utility has been demonstrated in brain-inspired computing (3,4) and hybrid CMOS/memristor logic circuits (5). Oxide-based memristors reported so far have shown a wide spectrum of complex switching current-voltage characteristics (6), ranging from bipolar nonlinear, bipolar linear, unipolar bistable, to the unipolar threshold switching. It is generally recognized (6,7) that the complex switching behavior in memristors is governed by temporally and spatially intertwined electrical and thermal processes of electrons, holes, and mobile vacancies, including field drift due to potential gradient, Fick diffusion due to concentration gradient, Soret effect due to temperature gradient, and Joule heating. Quite a few comprehensive models (8-12) have been published to enhance the understanding of switching physics in memristors. However, even these comprehensive models do not capture all of the important processes on a microscopic level: for example, Refs. 8-10 solve the microscopic drift diffusion equations for carriers, but completely ignore the very important Joule heating effects, while Refs. 11-12 model the Joule heating effects, but oversimplify the treatment of electron transport and the coupling between electron and vacancy transport. To the best of our knowledge, there has been *no reported work* that treats *simultaneously* the electrical transport of electrons, holes, and vacancies, and Joule heating thermal effects on a *microscopic* level in realistic 3D memristor geometries. In order to gain understanding of underlying physical switching mechanisms and accelerate the experimental development of oxide memristive

devices, a fully-coupled microscopic model is necessary and should be able to simulate the entire switching spectrum.

Fully-Coupled Transport Model

In this work, we present a fully-coupled electrical and thermal microscopic model that includes all the important processes and treats the transport of electrons, holes, and vacancies together with the Joule heating on an equal footing. Namely, we solve simultaneously the five coupled partial differential equations (PDEs):

$$\frac{\partial n}{\partial t} = \frac{1}{q}\nabla \bullet \vec{J}_n - R_{net} \quad [1]$$

$$\frac{\partial p}{\partial t} = -\frac{1}{q}\nabla \bullet \vec{J}_p - R_{net} \quad [2]$$

$$\frac{\partial n_V}{\partial t} = -\frac{1}{q}\nabla \bullet \vec{J}_V \quad [3]$$

$$\nabla \bullet \varepsilon_0 \varepsilon_r \nabla(\phi - \theta) = -q(p - n + n_V + C) \quad [4]$$

$$\frac{\partial}{\partial t}(c_L T) - \nabla \bullet (\kappa_L \nabla T) = H \quad [5]$$

Equations [1]-[3] are the time-dependent continuity equations governing the transport of electrons (denoted as n), holes (p), and oxygen vacancies (n_V), respectively. We assume oxygen vacancies are positive, singly charged particles throughout the paper for simplicity. R_{net} represents a net recombination rate due to all possible electron-hole generation/recombination processes, while possible reactions between oxygen vacancies and electrons/holes are neglected. The Poisson equation [4] captures the electrostatic effects from all charged species, where C represents a net positive charge from fixed dopants, i.e., $C = N_D^+ - N_A^-$, with N_D^+ being fixed donors, and N_A^- fixed acceptors. Note the left hand side of the Poisson equation uses (ϕ-θ) instead of ϕ alone, because ϕ here is chosen to be the intrinsic Fermi potential (i.e., negative of the intrinsic Fermi level), and θ is a band structure parameter and chosen such that (ϕ-θ) represents the vacuum potential. Specifically, θ is chosen to be the difference between vacuum energy level and intrinsic Fermi level, and given by

$$\theta = \frac{1}{q}\left[\chi + \frac{1}{2}E_g + \frac{1}{2}k_B T \ln\left(\frac{N_C}{N_V}\right)\right] \quad [6]$$

Where χ, E_g, N_C, and N_V are the electron affinity, band gap, electron effective density of states, and hole effective density of states, respectively, of the material used; T is the lattice temperature; q is the elemental charge; k_B is the Boltzmann constant. In a homo- or hetero-junction device with spatially varying temperature, vacuum potential satisfies the Poisson equation, however, solving the vacuum potential directly from the coupled PDEs often shows more numerical convergence problems (13). Hence a more robust and popular choice is to rewrite the equation as [4] and solve for the intrinsic Fermi potential,

which approach is also widely used in commercial TCAD codes (14). Equation [5] is the time-dependent Fourier heat equation which models the Joule heating effect.

The current densities for electrons, holes, and vacancies include contributions from the field drift due to potential gradient, Fick diffusion due to concentration gradient, and the Soret effect due to temperature gradient. They are given by Eqs. [7]-[9]:

$$\vec{J}_n = qn\mu_n \vec{E} + qD_n \nabla n + k_B n \mu_n \nabla T \quad [7]$$

$$\vec{J}_p = qp\mu_p \vec{E} - qD_p \nabla p - k_B p \mu_p \nabla T \quad [8]$$

$$\vec{J}_V = qn_V \vec{v}_V - qD_V \nabla n_V - qD_V S_V n_V \nabla T \quad [9]$$

Where $\vec{E} = -\nabla\phi$. Equations [7]-[8] are the standard drift-diffusion equations including temperature gradient for electrons and holes, and can be derived (15) from the well-known semiclassical Boltzmann transport equation under various assumptions. The electron (hole) mobility is related to the electron (hole) diffusion coefficient through the Einstein relation, i.e., $D_n / \mu_n = D_p / \mu_p = k_B T / q$. The three terms in Eq. [9] for the vacancy current density show the same signs as those of holes in [8], which is consistent with the assumption that vacancies and holes are both positively charged. The third term in Eq. [9] describes the Soret effect and is taken from Ref. 16. The models for the vacancy velocity, diffusion and Soret coefficients will be discussed in the subsection.

The heat generation in Eq. [5] can be modeled in different levels of sophistication (17-22). Since it is generally accepted that Joule heating is the most dominant heat generation source in memristive devices, we model the heat generation as

$$H = \left(\vec{J}_n + \vec{J}_p + \vec{J}_V \right) \bullet \vec{E} + R_{net}(E_g + 3k_B T) \quad [10]$$

which includes Joule heating due to all charge carriers and contribution from possible electron-hole recombination processes.

The fully-coupled equations with appropriate physical models and boundary conditions are implemented in *Charon* (23), an open-source TCAD code developed at Sandia National Labs. *Charon* supports both finite element and finite volume discretization. For finite element discretization, it provides several stabilization schemes including the SUPG (Streamline Upwinding Petrov-Galerkin) and EFFG (Exponentially Fitted Flux Galerkin) methods (24). *Charon* is built on the open-source *Trilinos* libraries (25) that provide cutting-edge capabilities for solving nonlinear PDEs, including discretization utilities, nonlinear and linear solvers, MPI parallel, automatic differentiation, and many more.

Vacancy Velocity and Soret Model

The velocity of vacancies in memristors is widely modeled using the rigid point ion model (12, 26, 27). However, the original model in Ref. 27 was proposed only for one

spatial dimension (1D), and subsequent papers also describe the model in 1D only. To extend the model to multi-dimensional applications, we apply the model in all spatial dimensions. That is, each component i ($i = x, y, z$) of the velocity is given by the rigid point model as

$$v_{V,i} = 2fa\exp\left(\frac{-E_a}{k_BT}\right)\sinh\left(\frac{qaE_i}{2k_BT}\right) = \mu_V E_c \sinh(E_i/E_c), i = x, y, z \quad [11]$$

Where f is the frequency of escape attempts, often in the range of 10^{12} -10^{13} Hz, and a is the periodicity of lattice sites, in the range of a few Angstroms, while E_a is the activation energy representing the energy barrier for ions/vacancies to hop over and its value varies significantly in literature; E_i is the ith-component of electric field; E_c denotes the critical field and is equal to $E_c = 2k_BT/(qa)$; μ_V denotes the ion mobility and is given by Eq. [12]. The vacancy diffusion coefficient is computed using Eq. [13].

$$\mu_V = \frac{qfa^2}{k_BT}\exp\left(\frac{-E_a}{k_BT}\right) \quad [12]$$

$$D_V = \frac{k_BT}{q}\mu_V = fa^2\exp\left(\frac{-E_a}{k_BT}\right) \quad [13]$$

It is clear from Eq. [11] that the vacancy velocity shows a very strong dependence on temperature and electric field. Figure 1 shows the vacancy velocity in 1D as a function of electric field at temperatures of 300 K to 1000 K in an interval of 100 K for a given set of parameters that f = 10^{12} Hz, a = 0.1 nm, E_a = 0.8 eV. It is seen that for temperatures of 300 K to 600 K, an increase of 100 K in temperature leads to several orders of increase in vacancy velocity, while for higher temperatures, the increase of vacancy velocity with temperature significantly slows down. On the other hand, the vacancy velocity increases linearly with electric field until the field exceeds a critical value, beyond which the velocity increases exponentially with field.

The Soret coefficient in Eq. [9] is modeled as $S_V = E_a/(k_BT^2)$. Here we want to point out that several papers (12,26) argue that the Soret coefficient should be negative for vacancies, i.e., $S_V = -E_a/(k_BT^2)$, implying that vacancies move from cold to hot regions. However, we think this argument is very debatable. It is well-known (28) that electrons in n-type semiconductors and holes in p-type semiconductors both move from hot to cold regions. We think vacancies should behave similar to holes, and it is more physical to assume that vacancies move from hot to cold regions, hence a positive Soret coefficient is used in this work.

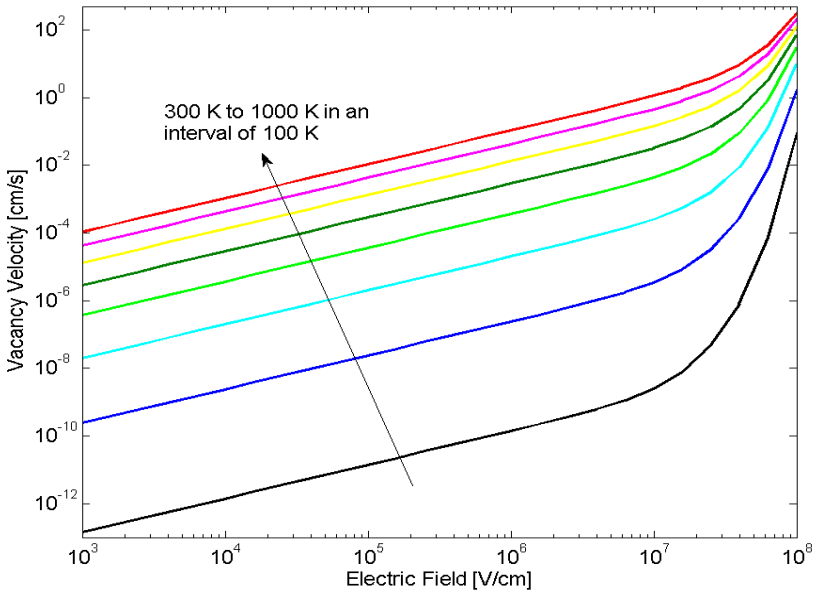

Figure 1. Vacancy velocity dependence on electric field and temperature for a given set of parameters that $f = 10^{12}$ Hz, $a = 0.1$ nm, $E_a = 0.8$ eV. Black arrow denotes the direction of temperature increasing from 300 K to 1000 K in an interval of 100 K.

Boundary Condition,

The boundary conditions (BCs) for electric potential, electron density, and hole density have two types: homogenous Neumann and Ohmic conditions. All non-Ohmic boundaries satisfy the homogenous Neumann condition, i.e., $\nabla\phi \bullet \hat{\eta} = \vec{J}_n \bullet \hat{\eta} = \vec{J}_p \bullet \hat{\eta} = 0$, where $\hat{\eta}$ denotes the outer normal of a boundary. Ohmic BC is determined by charge neutrality and thermal equilibrium conditions. Further assuming Maxwell-Boltzmann statistics, at Ohmic boundaries, we have

$$p_0 - n_0 + n_V + C = 0 \qquad [14]$$

$$E_{Fn} = E_{Fp} = E_F = -qV_a \qquad [15]$$

$$n_0 p_0 = n_{ie}^2 \qquad [16]$$

Where V_a is the applied voltage. The equilibrium electron and hole densities are given by

$$n_0 = N_C \exp\left(\frac{E_F - E_C}{k_B T}\right) \qquad [17]$$

$$p_0 = N_V \exp\left(\frac{E_V - E_F}{k_B T}\right) \qquad [18]$$

The conduction and valence band edges are related to the electric potential through the following expressions: $E_C = E_{vac} - \chi = q\theta - q\phi - \chi$ and $E_V = E_C - E_g$. Using these

relations and Eqs. [14]-[18], we can obtain the carrier densities and electric potential at Ohmic boundaries. Specifically, for n-type material, we have

$$n_0 = \frac{N_{eff}}{2} + \sqrt{\left(\frac{N_{eff}}{2}\right)^2 + n_{ie}^2}, N_{eff} = C + n_V \quad [19]$$

$$p_0 = \frac{n_{ie}^2}{n_0}, n_{ie} = \sqrt{N_C N_V}\exp\left(\frac{-E_g}{2k_B T}\right) \quad [20]$$

$$\phi = \frac{1}{q}(q\theta - \chi) + \frac{k_B T}{q}\ln(y) + V_a, y = \frac{N_{eff}}{2N_C} + \left[\left(\frac{N_{eff}}{2N_C}\right)^2 + \frac{N_V}{N_C}\exp\left(\frac{-E_g}{k_B T}\right)\right]^{1/2} \quad [21]$$

For p-type material, the corresponding expressions are

$$n_0 = \frac{n_{ie}^2}{p_0}, n_{ie} = \sqrt{N_C N_V}\exp\left(\frac{-E_g}{2k_B T}\right) \quad [22]$$

$$p_0 = \frac{-N_{eff}}{2} + \sqrt{\left(\frac{N_{eff}}{2}\right)^2 + n_{ie}^2}, N_{eff} = C + n_V \quad [23]$$

$$\phi = \frac{1}{q}(q\theta - \chi - E_g) - \frac{k_B T}{q}\ln(y) + V_a, y = \frac{-N_{eff}}{2N_V} + \left[\left(\frac{N_{eff}}{2N_V}\right)^2 + \frac{N_C}{N_V}\exp\left(\frac{-E_g}{k_B T}\right)\right]^{1/2} \quad [24]$$

The boundary condition for vacancies is homogenous Neumann condition for the simulation domain, i.e., $\vec{J}_V \bullet \hat{\eta} = 0$, indicating that the total number of vacancies in the domain is constant. For the temperature equation, temperature is a user-defined constant at Dirichlet boundaries, while $\nabla T \bullet \hat{\eta} = 0$ at all non-Dirichlet boundaries.

Results and Discussions

The above fully-coupled transport model is applied to simulate the switching process in a 3D filamentary tantalum oxide memristor shown in Fig. 2. Since the Ta electrode and conduction filament (CF) are the active regions, we solve the coupled electrical and thermal equations there, and allow the heat to conduct in the Ta_2O_5 and Pt regions. Voltage is applied to the top of Ta electrode, while the bottom of CF is grounded. The top and bottom surfaces of the structure are set to 300 K. The rigid point ion model is used to describe the movement of vacancies. Thermal and electrical parameters are being calibrated with experimental data as a function of temperature and vacancy density, and reasonable constant values are currently used for the results shown here.

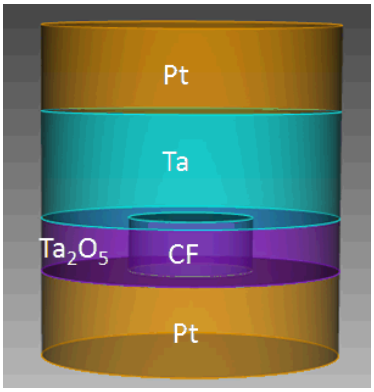

Figure 2. Structure of the 3D filamentary tantalum oxide memristor simulated. The conduction filament (CF) has a radius of 5 nm, and the Ta electrode has a radius of 12 nm. The CF is 5 nm thick, the Ta electrode is 10 nm thick, and the Pt electrode is 8 nm thick.

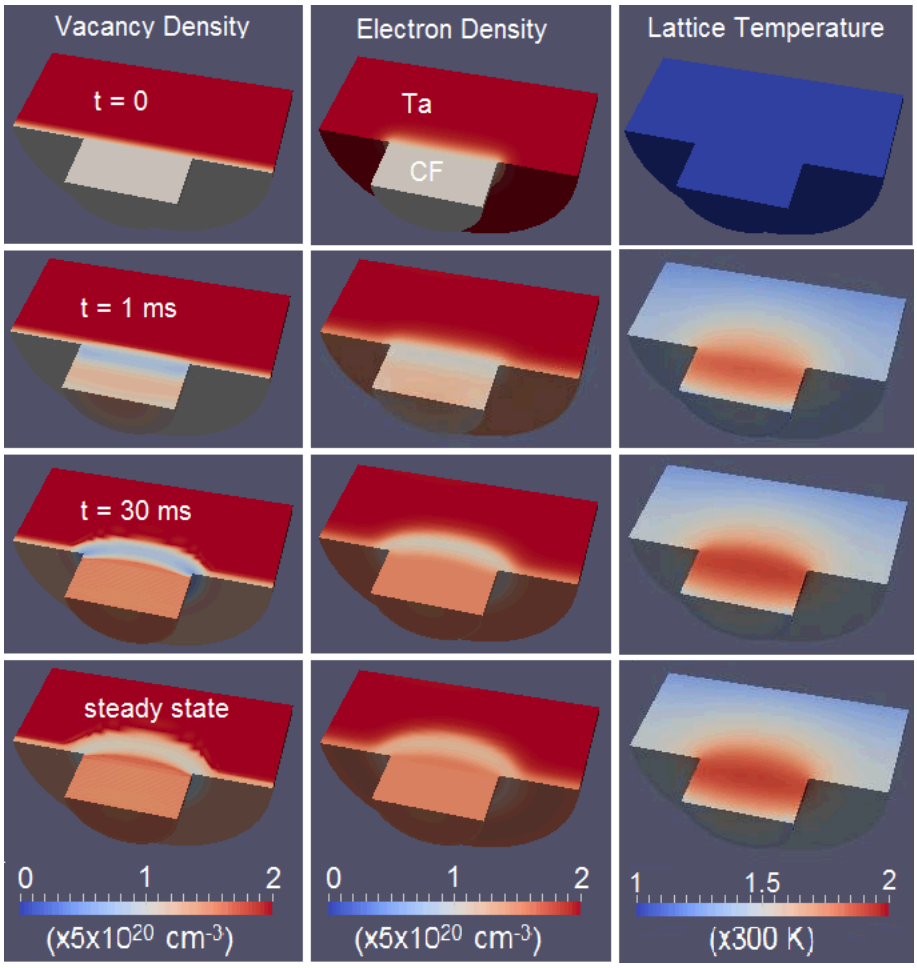

Figure 3. Center view of the simulated time evolution of vacancy density (left panel), electron density (middle panel), and lattice temperature (right panel) in the Ta and CF regions during ON switching

We first investigate the time evolution of carrier density and temperature when a memristor switches from OFF to ON state. Figure 3 shows center view of the simulated time evolution of vacancy density, electron density, and lattice temperature in the Ta and

CF regions during ON switching, when 1V is applied to the top of Ta electrode. The first row first column of Fig. 3 shows that the Ta electrode and CF regions have an initial uniform vacancy density of 1×10^{21} and 5×10^{20} cm^{-3} respectively, with a sharp Gaussian transition profile. The remaining of first row of Fig. 3 shows the initial electron density and the initial temperature at 300 K. With a positive voltage applied to the Ta electrode, Joule heating causes an increase of temperature, which is the strongest near the Ta/CF interface, causing vacancies from the Ta electrode to flow into the CF, as seen at 1ms (second row of Fig. 3).

As vacancies fill in the filament, the vacancy density in the CF keeps increasing. In order to prevent unphysical piling-up of vacancies at the bottom of CF, we modify the vacancy current density J_V in Eq. [9] to $J_V^* = J_V\left(1 - n_V / N_{\max}\right)$ in the code, where N_{max} represents the maximum available oxygen site concentration in the material that can accommodate vacancies. A similar approach was used in Ref. 9 to avoid unphysically large vacancy density. In our simulation, N_{max} is chosen to be 7.5×10^{20} cm^{-3}, with the reasoning that the CF region is less conductive than the Ta electrode even in the ON state. Using this self-limiting scheme, we observe that, as temperature further increases, vacancies continue filling in the CF, and the vacancy density is indeed limited to N_{max} in the filament. The CF is completely filled up around 30 ms (third row of Fig. 3), reaching the stage we call filament saturation. After that time, vacancies in the Ta electrode move to fill in the gap next to the filament, and eventually reach a steady-state distribution (fourth row of Fig. 3). It is seen that vacancies show a two-stage process during ON switching, i.e., filling in the filament, followed by reducing the gap in the Ta electrode. On the other hand, the electron density shows a time evolution process similar to vacancy density, indicating that vacancies indeed act as n-type mobile dopants. The temperature starts being the hottest at the CF/Ta interface, then increases with time and spreads further into the CF and Ta regions, and reaches around 600 K at steady state.

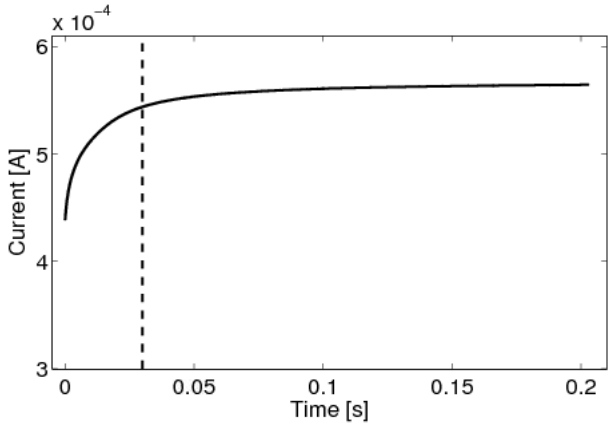

Figure 4. Time evolution of current for the ON switching process shown in Fig. 3. Dashed line indicates the time of 30 ms at which filament saturation is reached.

Figure 4 shows the time evolution of current for the ON switching process shown in Fig. 3. At 30 ms denoted by the dashed line, the CF is completely filled with vacancies and reaches saturation. It is seen that current increases most significantly before filament saturation, and increases only slightly after that, until it reaches steady state. From this particular current time evolution, we can make two observations: (i) the ON switching

process is very slow (it takes about 0.05 s to reach steady state); (ii) the ON-to-OFF current ratio is quite small, approximately 1.3.

To investigate the possibility of improving (i) and (ii), we conducted two additional simulations. The first one has the same simulation setup as that of Fig. 4, except that 1.5 V is applied to the Ta electrode. The simulation shows a time evolution of vacancy density, electron density, and temperature similar to Fig. 3, however, the peak temperature reaches 900 K compared to 600 K in Fig. 3, and more importantly, the current shows much faster time evolution. The current is plotted in logarithmic time as red dashed curve in Fig. 5. The black solid curve corresponds to that of Fig.4 in logarithmic time. Comparing the red dashed curve with the black solid curve, we see that a 50% increase in voltage results in about 50% increase in current (which is very reasonable when a memristive device works in the linear Ohmic regime), whereas it leads to about 3 orders of magnitude decrease in switching time. For the second simulation, we reduce the initial vacancy density in the CF by 2.5 times, such that the initial vacancy density ratio in the Ta and CF regions is equal to 5, and keep everything else the same as the previous (1.5 V) case. The resulting current versus time is plotted as blue dash-dot curve in Fig. 5. Comparing the blue dash-dot curve to the red dashed curve, we observe that, the steady-to-initial current ratio increases from about 1.3 (red curve) to 2.6 (blue curve), when the initial vacancy density in the CF is reduced by 2.5 times; on the other hand, the switching time and ON current are comparable for the blue and red curves. It is clear that the ON switching time is very sensitive to the voltage applied, and the ON-to-OFF current ratio strongly depends on the filament vacancy density in the OFF state.

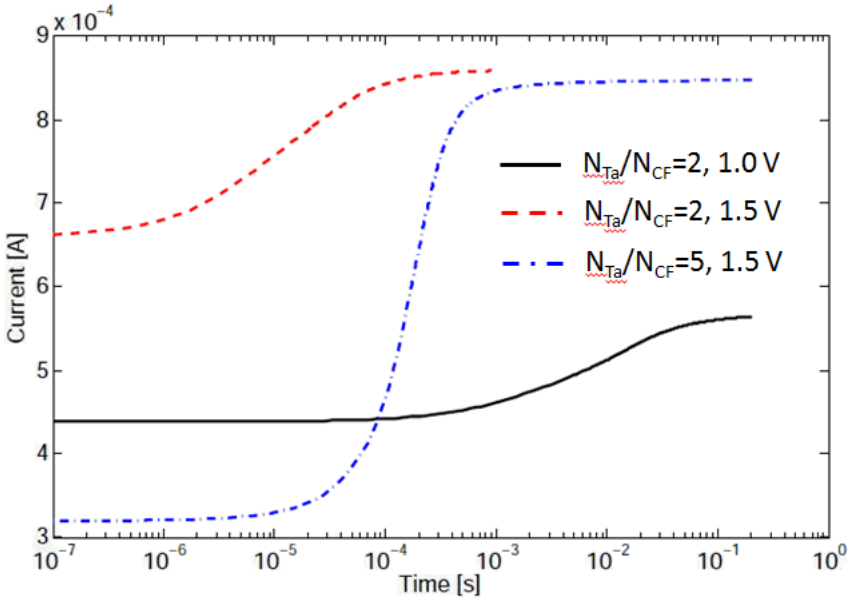

Figure 5. Time evolution of current during ON switching. Black solid curve – initial vacancy density ratio in the Ta and CF regions equals to 2 and 1 V is applied; red dashed curve – initial vacancy density ratio is 2 and 1.5 V is applied; blue dash-dot curve – initial vacancy density ratio is 5 and 1.5 V is applied.

Conclusions

We present a fully-coupled electrical and thermal transport model for oxide memristors that solves simultaneously the time-dependent continuity equations for electrons, holes, and mobile vacancies, together with the time-dependent temperature heat equation. The model captures all the important processes that drive memristive switching, including field drift, Fick diffusion, Soret effect, and Joule heating. The model is applied to simulate the ON switching in a 3D filamentary TaOx memristor. Simulation results show that vacancies fill in the conduction filament till saturation and then fill out a gap formed in the Ta electrode during ON switching, when the OFF-state vacancy density has a different uniform distribution in the conduction filament and the Ta electrode. Furthermore, ON-switching time shows an exponentially strong dependence on applied voltage, while the ON-to-OFF resistance ratio demonstrates high sensitivity to the filament vacancy density in the OFF state. The generality of the proposed model allows to simulate and investigate the underlying physical switching mechanisms in a wide spectrum of oxide memristors ranging from field-dominant, field-thermal-driven, to thermal-dominant memristive devices.

Acknowledgments

This work was supported by the Laboratory Directed Research and Development program at Sandia National Laboratories. Sandia is a multiprogram laboratory operated by Sandia Corporation, a Lockheed Martin Company, for the United States Department of Energy's National Nuclear Security Administration under Contract DE-AC04-94AL85000. The authors greatly acknowledge the numerous helpful discussions on coding and physics from our colleagues Larry Musson and Gary Hennigan. We also sincerely thank Pavel Bochev, John Shadid, and Andy Huang for their insightful discussions on PDE discretization and stabilization. We owe special thanks to Eric Cyr and Stephen Bond for their work with *Panzer*, which is the foundation of *Charon* and makes it possible to implement our fully coupled model in *Charon*. Acknowledgement also goes to our colleagues Harold Hjalmarson and Brian Tierney for helpful discussions.

References

1. Proceedings of the IEEE (special issue)*: Memristors: Devices, Models, and Applications*, **100**(6) (2012).
2. P. R. Mickel, A. J. Lohn and M. J. Marinella, *Modern Physics Letters B*, **28**(10) (2014).
3. S. H. Jo, T. Chang, I. Ebong, B. B. Bhadviya, P. Mazumder, and W. Lu, *Nano Lett.*, **10**(4), 1297 (2010).
4. K. H. Kim, S. Gaba, D. Wheeler, J. M. Cruz-Albrecht, T. Hussain, N. Srinivasa, and W. Lu, *Nano Lett.,* **12**(1), 389 (2012).
5. D. Sacchetto, G. De Micheli, and Y. Leblebici, *Proc. of the IEEE*, **100**(6), 2008 (2012).
6. J. J. Yang, D. B. Strukov, and D. R. Stewart, *Nature Nanotech.*, **8**, 13 (2013).
7. D. S. Jeong, R. Thomas, R. S. Katiyar, J. F. Scott, H. Kohlstedt, A. Petraru, and C. S. Hwang, *Rep. Prog. Phys*., **75**, 076502 (2012).

8. D. B. Strukov, J. L. Borghetti, and R. S. Williams, *small*, **5**(9), 1058 (2009).
9. M. Noman, W. Jiang, P. A. Salvador, M. Skowronski, and J. A. Bain, *Appl. Phys. A*, **102**, 877 (2011).
10. J. D. Greenlee, J. C. Shank, M. B. Tellekamp, and W. A. Doolittle, *J. Appl. Phys.*, **114**, 034504 (2013).
11. S. Larentis, F. Nardi, S. Balatti, D. C. Gilmer, and D. Ielmini, *IEEE Trans. Electron Devices*, **59**(9), 2468 (2012).
12. S. Kim, S. Choi, and W. Lu, *ACS Nano*, **8** (3), 2369 (2014).
13. X. Gao, E. Nielsen, R. P. Muller, R. W.Young, A. G. Salinger, N. C. Bishop, M. P. Lilly, and M. S. Carroll, *J. Appl. Phys.*, **114**, 164302 (2013).
14. Synopsys Inc., *Taurus Medici User Guide*, Version Y-2006.06, June 2006.
15. M. Lundstrom, *Fundamentals of Carrier Transport*, p. 236, Cambridge University Press, Cambridge (2000).
16. D. B. Strukov, F. Alibart, and R. S. Williams, *Appl. Phys. A*, **107**, 509 (2012).
17. S. P. Gaur and D. H. Navon, *IEEE Trans. Electron Devices*, **ED-23**(1), 50 (1976).
18. M. S. Adler, *IEEE Trans. Electron Devices*, **ED-25**(1), 16 (1978).
19. A. Chryssafis and W. Love, *Solid-State Electronics*, **22**, 249 (1979).
20. G. K. Wachutka, *IEEE Trans. CAD*, **9**(11), 1141 (1990).
21. U. Lindefelt, *J. Appl. Phys.* **75**, 942 (1994).
22. J. E. Parrott, *IEEE Trans. Electron Devices*, **43**(5), 809 (1996).
23. G. Hennigan, D. Fixel, J. Castro, and P. Lin, *Charon Parallel Semiconductor Device Simulator*, Sandia Technical Report, SAND2010-3905 (2010).
24. P. Bochev and K. Peterson, *Cent. Eur. J. Math.*, **11**(8), 1458 (2013).
25. https://trilinos.org/.
26. D. B. Strukov and R. S. Williams, *Appl. Phys. A*, **94**, 515 (2009).
27. N. Cabrera and N. F. Mott, *Rep. Prog. Phys.,* **12**, 163 (1948).
28. T. M. Tritt and M. A. Subramanian, *MRS Bulletin*, **31**, 188 (2006).